PCCP

Accepted Manuscript

ROYAL SOCIETY OF CHEMISTRY

www.rsc.org/pccp

Quantum transport through a Coulomb blockaded quantum emitter coupled to a plasmonic dimer

A. Goker and H. Aksu
Department of Physics,
Bilecik University,
11210, Gülümbe, Bilecik, Turkey
(Dated: December 7, 2015)

We study the electron transmission through a Coulomb blockaded quantum emitter coupled to metal nanoparticles possessing plasmon resonances by employing the time-dependent non-crossing approximation. We find that the coupling of the nanoparticle plasmons with the excitons results in a significant enhancement of the conductance through the discrete state with the higher energy beyond the unitarity limit while the other discrete state with the lower energy remains Coulomb blockaded. We show that boosting plasmon-exciton coupling well below the Kondo temperature increases the enhancement adding another quantum of counductance upon saturation. Finite bias and increasing emitter resonance energy tends to reduce this enhancement. We attribute these observations to the opening of an additional transport channel via the plasmon-exciton coupling.

I. INTRODUCTION

Concentrating optical energy like a lens into spatial regions much smaller than the wavelength of the light has been in high demand for a long time to be able to keep up with the ever shrinking size of the state-of-the-art electronic devices and design high performance miniature optoelectronic components. Realization of tunable plasmon resonances in metal nanoparticles via optical excitations[1] provided a major breakthrough towards this end. These plasmon resonances generate tremendeous field enhancements around the metal nanoparticles.[2] This feature opens a new avenue by enabling coupling between the metal nanoparticles and nearby quantum impurities like dots or molecules.

An entangled two level quantum emitter located between two plasmonic nanoparticles can be considered as a prototype for a two qubit quantum computer.[3] Therefore, it is of great interest to understand how a direct coupling of nanoparticle plasmons with the excitons in the quantum emitter influences the spin dependent electron transport through this device. The term plexcitonics has been coined for the hybrid light-matter states involving plasmon-exciton couplings[4] and it is thought to be the first stride towards future tunable molecular systems[5] and plasmonic switches.[6]

Observation of the Fano resonance in plexcitonic systems[7] necessitated the development of a full quantum theory for electron transport across such a junction by taking into account the electron spin and the Coulomb interaction explicitly. Initial attempts utilized time-dependent density functional theory[8] and a semiclassical model involving incorporation of quantum coherent electron tunnelling into a classical electromagnetic framework[9] by completely ignoring the plasmon-exciton coupling and spin effects. Subsequent studies employed more intricate Green function methods to demonstrate that only the dipolar plasmon mode is rel-

evant in the strong coupling regime.[10] Same method has been used to investigate the exciton transfer through a collection[11] and a chain[12] of quantum emitters near a metallic nanoparticle.

Despite all these efforts, incorporation of strong electron correlations into plexcitonics by accounting for the electron spin remains missing to this day. We recently developed a many-body Green function theory for this system and showed that the Fano resonance arising due to the plasmon-exciton coupling is quenched for a Coulomb blockaded quantum emitter above the Kondo temperature of the discrete state with the higher energy.[13] In this paper, we will extend this formalism and investigate for the first time how strong electron correlations alter the electron transport for a Coulomb blockaded plexcitonic junction. It has already been shown that the plasmon-induced oscillating field within a single-molecule junction can boost the conductance outside the Coulomb blockade regime.[14] Here, we will demonstrate for the first time that the conductance can also be significantly enhanced with a finite plasmon-exciton coupling at sufficiently low temperatures where the Coulomb blockade can be lifted with an exquisite many-body phenomenon called the Kondo effect.

II. THEORY

We consider a system comprised of a quantum emitter which can be represented by two discrete states located between two metal nanoparticles possessing plasmon resonances. This quantum emitter corresponds to a parallel-coupled double quantum dot in reality. A schematic illustration of this physical system is shown in Fig. 1. We can describe this system with the Hamiltonian given by

$$H = H_N + H_{EN} + \sum_{\alpha \in \{E, rad\}} (H_\alpha + V_\alpha). \quad (1)$$

Here, H_N models the metal nanoparticles as

$$H_N = \sum_{K \in \{L,R\}, \sigma} \varepsilon_{K\sigma} c_{K\sigma}^\dagger c_{K\sigma} + \sum_{K \in \{L,R\}} \varepsilon_{pK} b_K^\dagger b_K \quad (2)$$

and H_{EN} corresponds to the plasmon-exciton coupling

$$H_{EN} = \sum_{K \in \{L,R\}, \sigma} \left(\Delta_K x_\sigma^\dagger b_K + h.c. \right). \quad (3)$$

H_E describes the quantum emitter as

$$\begin{aligned} H_E &= \sum_{s \in \{g,e\}, \sigma} \varepsilon_s c_{s\sigma}^\dagger c_{s\sigma} + J \sum_\sigma (x_\sigma + h.c.) \\ &+ \frac{U}{2} \sum_{s \in \{g,e\}} n_{s\sigma} n_{s\sigma'}, \end{aligned} \quad (4)$$

whereas V_E describes the electron tunneling between the quantum emitter and the metal nanoparticles

$$V_E = \sum_{K \in \{L,R\}, \sigma} \left(V_{K,g(e)} c_{K\sigma}^\dagger c_{g(e)\sigma} + h.c. \right). \quad (5)$$

The radiation field is introduced via

$$H_{rad} = \sum_\alpha \varepsilon_\alpha a_\alpha^\dagger a_\alpha \quad (6)$$

and the coupling between the radiation field and the dipolar plasmons of each nanoparticle is given by

$$V_{rad} = \sum_{K \in \{L,R\}, \alpha} \left(W_{\alpha,K} a_\alpha^\dagger b_K + h.c. \right). \quad (7)$$

In these expressions, $c_{K\sigma}^\dagger (c_{K\sigma})$ is the creation(annihilation) operator for free electrons with spin σ in the metal nanoparticles while $c_{s\sigma}^\dagger (c_{s\sigma})$ is the electron creation(annihilation) operator in each spin degenerate discrete state within the quantum emitter. These spin degenerate states are denoted with $|g>$ and $|e>$ whose energy difference is $|\varepsilon_e - \varepsilon_g|$. ε_α is the energy of the radiation field with mode α and ε_{pK} is the plasmon energy in the left($K=L$) and right($K=R$) metal nanoparticle. The amplitudes appearing in the fourth and sixth term J and $V_{K,g(e)}$ are the electron tunneling (electron transfer) between the states $|g>$ and $|e>$ and between the metal nanoparticles and the state $|s \in \{g,e\}>$ respectively. Besides, $W_{\alpha,K}$ and Δ_K denote the amplitudes of coupling between the radiation field with mode α and the dipolar plasmons of each nanoparticle and between the exciton and the same dipolar plasmon modes. To simplify the equations above we denote the exciton annihilation and creation operators by x_σ and $x_\sigma^\dagger$ respectively,

$$\begin{aligned} x_\sigma &= c_{g\sigma}^\dagger c_{e\sigma} \\ x_\sigma^\dagger &= c_{e\sigma}^\dagger c_{g\sigma}. \end{aligned} \quad (8)$$
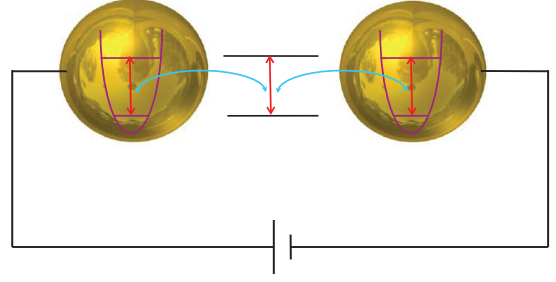

FIG. 1: This figure shows a schematic illustration of a plasmonic dimer consisting of two metal nanoparticles coupled to an excitonic quantum emitter.

Finally, the Coulomb repulsion energy within the discrete states $|g>$ and $|e>$ is denoted as U term while the number operator is denoted as $n_{s\sigma}$.

Typically, U term in the Hamiltonian overwhelms the other energy scales in this model owing to the confinement of the electrons within each state. This condition leads to $U \to \infty$ which forbids double occupancy on both discrete states. We will deal with this situation by writing the electron operators acting on the states $|g>$ and $|e>$ in terms of a pseudofermion and a massless boson as

$$\begin{aligned} c_{g(e)\sigma} &= b_{g(e)}^\dagger f_{g(e)\sigma} \\ c_{g(e)\sigma}^\dagger &= f_{g(e)\sigma}^\dagger b_{g(e)}, \end{aligned} \quad (9)$$

subject to the condition

$$Q_{B,g(e)} = b_{g(e)}^\dagger b_{g(e)} + \sum_\sigma f_{g(e)\sigma}^\dagger f_{g(e)\sigma} = 1. \quad (10)$$

Now we can also write $x_{m\sigma}^\dagger (x_{m\sigma})$ exciton creation(annihilation) operators in terms of the slave-boson representation as

$$\begin{aligned} x_\sigma &= f_{g\sigma}^\dagger b_g b_e^\dagger f_{e\sigma} \\ x_\sigma^\dagger &= f_{e\sigma}^\dagger b_e b_g^\dagger f_{g\sigma}, \end{aligned} \quad (11)$$

This restriction ensures that the occupancy of $|g>$ and $|e>$ is unity. This allows us to remove the U term from H_E and we end up with

$$H_E = \sum_{s \in \{g,e\}, \sigma} \varepsilon_s f_{s\sigma}^\dagger f_{s\sigma} + J \sum_\sigma (x_\sigma + h.c.). \quad (12)$$

Moreover, the electron tunneling between the quantum emitter and the metal nanoparticles becomes

$$V_E = \sum_{K \in \{L,R\}, \sigma} \left(V_{K,g(e)} c_{K\sigma}^\dagger b_{g(e)}^\dagger f_{g(e)\sigma} + h.c. \right) \quad (13)$$

Following previous work[13,15], we assume that the incident laser is perpendicular to the axis connecting the metal nanoparticles. In this case, the metal nanoparticles absorb the photons of the incident laser in the same phase. Furthermore, we assume that the incident laser is not directly coupled to the quantum emitter and the sole pumping of the system occurs via a single laser mode ε_0 which only excites the dipolar plasmon mode of the metal nanoparticles. Hence, the role of the plasmonic dimer is to store the energy delivered by the radiation field and transfer it to the quantum emitter via plasmon-exciton coupling. J term in H_E will be dropped in this situation since the quantum emitter is not allowed to absorb energy directly from the laser. These assumptions enable us to take the dipolar plasmon energy of each nanoparticle equal as $\varepsilon_{pL} = \varepsilon_{pL} = \varepsilon_p$. Similarly, symmetrical plasmon-exciton and plasmon-laser couplings will be considered such that $\Delta_L = \Delta_R = \Delta$ and $W_{0,L} = W_{0,R} = W_0$.

In order to investigate the nonequilibrium dynamics of this system, we invoke the time-ordered double-time Green functions defined as

$$
\begin{aligned}
iG_{g(e)}(t,t') &= < T_c f_{g(e)\sigma}(t) f^\dagger_{g(e)\sigma}(t') > \\
iB_{g(e)}(t,t') &= < T_c b_{g(e)}(t) b^\dagger_{g(e)}(t') >,
\end{aligned} \tag{14}
$$

where the time ordering operator T_c acts along the Kadanoff-Baym contour. The analytic pieces of these Green functions are given

$$
\begin{aligned}
iG_{g(e)}(t,t') &= \theta(t-t')G^>_{g(e)}(t,t') - \theta(t'-t)G^<_{g(e)}(t,t') \\
iB_{g(e)}(t,t') &= \theta(t-t')B^>_{g(e)}(t,t') + \theta(t'-t)B^<_{g(e)}(t,t')
\end{aligned} \tag{15}
$$

In these expressions, the lesser Green functions can be written in terms of the pseudofermion and slave boson operators as $G^<_{g(e)}(t,t') = < f^\dagger_{g(e)\sigma}(t') f_{g(e)\sigma}(t) >$ and $B^<_{g(e)}(t,t') = < b^\dagger_{g(e)}(t') b_{g(e)}(t) >$ whereas the greater ones are $G^>_{g(e)}(t,t') = < f_{g(e)\sigma}(t) f^\dagger_{g(e)\sigma}(t') >$ and $B^>_{g(e)}(t,t') = < b_{g(e)}(t) b^\dagger_{g(e)}(t') >$. We can also write the retarded Green functions by combining these analytic pieces as

$$
\begin{aligned}
G^r_{g(e)}(t,t') &= -i\theta(t-t')[G^>_{g(e)}(t,t') + G^<_{g(e)}(t,t')] \\
B^r_{g(e)}(t,t') &= -i\theta(t-t')[B^>_{g(e)}(t,t') - B^<_{g(e)}(t,t')]
\end{aligned} \tag{16}
$$

Since the plasmon-exciton coupling strength is typically two orders of magnitude smaller than the electron-electron interactions within the quantum emitter, it is possible to approach this problem by treating the plasmon-exciton coupling perturbatively. This can be accomplished by setting up Dyson equations for $B^r_{g(e)}$, $G^r_{g(e)}$ and $B^<_{g(e)}$, $G^<_{g(e)}$. These equations can be explicitly written as

$$
\left(i\frac{\partial}{\partial t} - \varepsilon_{g(e)}\right) G^r_{g(e)}(t,t') = \delta(t-t') + \int_{-\infty}^{\infty} dt_1 \Sigma^r_{g(e)}(t,t_1) G^r_{g(e)}(t_1,t') \tag{17}
$$

$$
i\frac{\partial}{\partial t} B^r_{g(e)}(t,t') = \delta(t-t') + \int_{-\infty}^{\infty} dt_1 \Pi^r_{g(e)}(t,t_1) B^r_{g(e)}(t_1,t') \tag{18}
$$

$$
\left(i\frac{\partial}{\partial t} - \varepsilon_{g(e)}\right) G^<_{g(e)}(t,t') = \int_{-\infty}^{\infty} dt_1 \Sigma^r_{g(e)}(t,t_1) G^<_{g(e)}(t_1,t') + \int_{-\infty}^{\infty} dt_1 \Sigma^<_{g(e)}(t,t_1) G^a_{g(e)}(t_1,t') \tag{19}
$$

$$
i\frac{\partial}{\partial t} B^<_{g(e)}(t,t') = \int_{-\infty}^{\infty} dt_1 \Pi^r_{g(e)}(t,t_1) B^<_{g(e)}(t_1,t') + \int_{-\infty}^{\infty} dt_1 \Pi^<_{g(e)}(t,t_1) B^a_{g(e)}(t_1,t') \tag{20}
$$

The pseudofermion and slave-boson self energies are required to solve these integro-differential equations. We invoke the non-crossing approximation (NCA) to express the self-energies and project them into $Q_{B,g(e)} = 1$ subspace. Dynamical quantities can be obtained quite accurately via NCA with the exception of very low temperatures and finite magnetic field. The details of our self-energy calculations are presented in appendix A extensively. Upon introducing[16,17]

$$
\begin{aligned}
B^r_{g(e)}(t,t') &= -i\theta(t-t')\left[B^>_{g(e)}(t,t') - B^<_{g(e)}(t,t')\right] \\
&:= -i\theta(t-t')b_{g(e)}(t,t')
\end{aligned} \tag{21}
$$

and

$$
\begin{aligned}
G^r_{g(e)}(t,t') &= -i\theta(t-t')\left[G^>_{g(e)}(t,t') + G^<_{g(e)}(t,t')\right] \\
&:= -i\theta(t-t')g_{g(e)}(t,t'),
\end{aligned} \tag{22}
$$

the Dyson equations for pseudofermion Green functions expressed in terms of the projected self-energies turn out to be

$$
\left(\frac{\partial}{\partial t} + i\varepsilon_g\right) g_g(t,t') = \\
-\int_{t'}^{t} dt_1 K^>(t,t_1)\tilde{b}_g(t,t_1)g_g(t_1,t') \\
-\int_{t'}^{t} dt_1 \mid \Delta \mid^2 \tilde{g}_e(t,t_1)\tilde{b}_g(t,t_1)\tilde{B}^<_e(t_1,t) \\
\times P^<(t_1,t)g_g(t_1,t') \tag{23}
$$

and

$$
\left(\frac{\partial}{\partial t} + i\varepsilon_e\right) g_e(t,t') = \\
-\int_{t'}^{t} dt_1 K^>(t,t_1)\tilde{b}_e(t,t_1)g_e(t_1,t') \\
-\int_{t'}^{t} dt_1 \mid \Delta \mid^2 \tilde{g}_g(t,t_1)\tilde{b}_e(t,t_1)\tilde{B}^<_g(t_1,t) \\
\times P^>(t,t_1)g_e(t_1,t') \tag{24}
$$

Similarly, slave-boson Green functions can be determined by solving the Dyson equations which are written employing the projected self-energies as

$$
\begin{aligned}
\frac{\partial}{\partial t} b_g(t,t') = &-\int_{t'}^{t} dt_1 K^<(t_1,t)\tilde{g}_g(t,t_1)b_g(t_1,t') \\
&-\int_{t'}^{t} dt_1 \mid \Delta \mid^2 \tilde{g}_g(t,t_1)\tilde{b}_e(t,t_1)\tilde{G}_e^<(t_1,t) \\
&\times P^>(t,t_1)b_g(t_1,t') \\
&+\int_{t'}^{t} dt_1 \mid \Delta \mid^2 \tilde{g}_g(t,t_1)\tilde{B}_e^<(t,t_1)\tilde{g}_e(t_1,t) \\
&\times P^<(t,t_1)b_g(t_1,t') \\
&-\int_{t'}^{t} dt_1 \mid \Delta \mid^2 \tilde{g}_g(t,t_1)\tilde{B}_e^<(t,t_1)\tilde{g}_e(t_1,t) \\
&\times P^>(t,t_1)b_g(t_1,t') \\
&+\int_{t'}^{t} dt_1 \mid \Delta \mid^2 \tilde{g}_g(t,t_1)\tilde{B}_e^<(t,t_1)\tilde{g}_e(t_1,t) \\
&\times P(t,t_1)b_g(t_1,t').
\end{aligned} \tag{25}
$$

and

$$
\begin{aligned}
\frac{\partial}{\partial t} b_e(t,t') = &-\int_{t'}^{t} dt_1 K^<(t_1,t)\tilde{g}_e(t,t_1)b_e(t_1,t') \\
&-\int_{t'}^{t} dt_1 \mid \Delta \mid^2 \tilde{g}_e(t,t_1)\tilde{b}_g(t,t_1)\tilde{G}_g^<(t_1,t) \\
&\times P^<(t_1,t)b_e(t_1,t') \\
&+\int_{t'}^{t} dt_1 \mid \Delta \mid^2 \tilde{g}_e(t,t_1)\tilde{B}_g^<(t,t_1)\tilde{g}_g(t_1,t) \\
&\times P^>(t_1,t)b_e(t_1,t') \\
&-\int_{t'}^{t} dt_1 \mid \Delta \mid^2 \tilde{g}_e(t,t_1)\tilde{B}_g^<(t,t_1)\tilde{g}_g(t_1,t) \\
&\times P^<(t_1,t)b_e(t_1,t') \\
&-\int_{t'}^{t} dt_1 \mid \Delta \mid^2 \tilde{g}_e(t,t_1)\tilde{B}_g^<(t,t_1)\tilde{g}_g(t_1,t) \\
&\times P(t_1,t)b_e(t_1,t').
\end{aligned} \tag{26}
$$

In these equations, the Green functions with a tilde on top are part of the self-energy terms and are calculated in the absence of any coupling between the discrete states $\mid g >$ and $\mid e >$. We want to emphasize that this decoupling scheme is required by the projection procedure in appendix A which closely follows the earlier NCA treatment of two impurity Kondo problem.[17] In essence, the only coupling mechanism between the states $\mid g >$ and $\mid e >$ consists of the plasmon-exciton interaction in our model. Therefore, inserting the Green functions that are calculated in the presence of the plasmon-exciton coupling into the self-energy terms would cause double counting problem because the plasmon-exciton coupling is already accounted for in Dyson equations.

After solving the above mentioned Dyson equations for the pseudofermion and slave-boson reterdad Green functions, we need to solve the related lesser Green functions

for the pseudofermion and slave-boson propagator using the Dyson equations given by

$$
\begin{aligned}
\left(\frac{\partial}{\partial t} + i\varepsilon_g\right) G_g^<(t,t') = \\
&-\int_{-\infty}^{t} dt_1 K^>(t,t_1)\tilde{b}_g(t,t_1)G_g^<(t_1,t') \\
&-\int_{-\infty}^{t} dt_1 \mid \Delta \mid^2 \tilde{g}_e(t,t_1)\tilde{b}_g(t,t_1)\tilde{B}_e^<(t_1,t) \\
&\times P^<(t_1,t)G_g^<(t_1,t') \\
&+\int_{-\infty}^{t'} dt_1 K_L^<(t,t_1)\tilde{B}_g^<(t,t_1)g_g(t_1,t') \\
&+\int_{-\infty}^{t'} dt_1 \mid \Delta \mid^2 G_e^<(t,t_1)\tilde{B}_g^<(t,t_1)\tilde{b}_e(t_1,t) \\
&\times P^>(t_1,t)g_g(t_1,t')
\end{aligned} \tag{27}
$$

$$
\begin{aligned}
\left(\frac{\partial}{\partial t} + i\varepsilon_e\right) G_e^<(t,t') = \\
&-\int_{-\infty}^{t} dt_1 K^>(t,t_1)\tilde{b}_e(t,t_1)G_e^<(t_1,t') \\
&-\int_{-\infty}^{t} dt_1 \mid \Delta \mid^2 \tilde{g}_g(t,t_1)\tilde{b}_e(t,t_1)\tilde{B}_g^<(t_1,t) \\
&\times P^>(t,t_1)G_e^<(t_1,t') \\
&+\int_{-\infty}^{t'} dt_1 K_R^<(t,t_1)\tilde{B}_e^<(t,t_1)g_e(t_1,t') \\
&+\int_{-\infty}^{t'} dt_1 \mid \Delta \mid^2 \tilde{G}_g^<(t,t_1)\tilde{B}_e^<(t,t_1)\tilde{b}_g(t_1,t) \\
&\times P^<(t,t_1)g_e(t_1,t')
\end{aligned} \tag{28}
$$

and

$$\frac{\partial}{\partial t} B_g^<(t,t') = -\int_{-\infty}^t dt_1 K^<(t_1,t)\tilde{g}_g(t,t_1)B_g^<(t_1,t')$$
$$-\int_{-\infty}^t dt_1 \mid \Delta \mid^2 \tilde{g}_g(t,t_1)\tilde{b}_e(t,t_1)\tilde{G}_e^<(t_1,t)$$
$$\times P^>(t,t_1)B_g^<(t_1,t')$$
$$+\int_{-\infty}^t dt_1 \mid \Delta \mid^2 \tilde{g}_g(t,t_1)\tilde{B}_e^<(t,t_1)\tilde{g}_e(t_1,t)$$
$$\times P^<(t,t_1)B_g^<(t_1,t')$$
$$-\int_{-\infty}^t dt_1 \mid \Delta \mid^2 \tilde{g}_g(t,t_1)\tilde{B}_e^<(t,t_1)\tilde{g}_e(t_1,t)$$
$$\times P^>(t,t_1)B_g^<(t_1,t')$$
$$+\int_{-\infty}^t dt_1 \mid \Delta \mid^2 \tilde{g}_g(t,t_1)\tilde{B}_e^<(t,t_1)\tilde{g}_e(t_1,t)$$
$$\times P(t,t_1)B_g^<(t_1,t')$$
$$+\int_{-\infty}^{t'} dt_1 K_L^>(t_1,t)\tilde{G}_g^<(t,t_1)b_g(t_1,t')$$
$$+\int_{-\infty}^{t'} dt_1 \mid \Delta \mid^2 \tilde{B}_e^<(t,t_1)\tilde{G}_g^<(t,t_1)\tilde{g}_e(t_1,t)$$
$$\times P^<(t,t_1)b_g(t_1,t') \qquad (29)$$

$$\frac{\partial}{\partial t} B_e^<(t,t') = -\int_{-\infty}^t dt_1 K^<(t_1,t)\tilde{g}_e(t,t_1)B_e^<(t_1,t')$$
$$-\int_{-\infty}^t dt_1 \mid \Delta \mid^2 \tilde{g}_e(t,t_1)\tilde{b}_g(t,t_1)\tilde{G}_g^<(t_1,t)$$
$$\times P^<(t_1,t)B_e^<(t_1,t')$$
$$+\int_{-\infty}^t dt_1 \mid \Delta \mid^2 \tilde{g}_e(t,t_1)\tilde{B}_g^<(t,t_1)\tilde{g}_g(t_1,t)$$
$$\times P^>(t_1,t)B_e^<(t_1,t')$$
$$-\int_{-\infty}^t dt_1 \mid \Delta \mid^2 \tilde{g}_e(t,t_1)\tilde{B}_g^<(t,t_1)\tilde{g}_g(t_1,t)$$
$$\times P^<(t_1,t)B_e^<(t_1,t')$$
$$-\int_{-\infty}^t dt_1 \mid \Delta \mid^2 \tilde{g}_e(t,t_1)\tilde{B}_g^<(t,t_1)\tilde{g}_g(t_1,t)$$
$$\times P(t_1,t)B_e^<(t_1,t')$$
$$+\int_{-\infty}^{t'} dt_1 K_R^>(t_1,t)\tilde{G}_e^<(t,t_1)b_e(t_1,t')$$
$$+\int_{-\infty}^{t'} dt_1 \mid \Delta \mid^2 \tilde{B}_g^<(t,t_1)\tilde{G}_e^<(t,t_1)\tilde{g}_g(t_1,t)$$
$$\times P^>(t_1,t)b_e(t_1,t'), \qquad (30)$$

where we again used the projected self-energies obtained in appendix A. Plasmon Green functions are obtained by solving the Dyson equation for the plasmon Green function using the method described previously[13] and plugged into the above Dyson equations. The values of all

Green functions are kept in a square matrix whose size is gradually increased until the values converge. Consequently, it is imperative that the matrix size of the plasmon Green functions is equal to the matrix size of the pseudofermion and slave boson Green functions. The explicit discretization and solution algorithm of the Dyson equations have been discussed in a detailed way previously.[18]

The influence of the ambient temperature is encoded in the Dyson equations explicitly through the Kernels given by Eq. A15 and implicitly through the pseudofermion and slave boson Green functions with a tilde on top which are calculated by utilizing the same Kernels. Moreover, the ambient temperature is also implicitly built into the plasmon Green functions which are determined by employing the same pseudofermion and slave boson Green functions with a tilde on top.[13]

Kondo effect is a quite subtle many-body effect that emerges when the discrete energy levels $\mid g >$ and $\mid e >$ lie below the Fermi level of the metal nanoparticles ε_f. It manifests itself in the density of states of each discrete level at sufficiently low temperatures as a very sharp resonance located slightly above the Fermi level of the metal nanoparticles ε_f with a linewidth on the order of

$$T_{K,g(e)} \propto \left(\frac{D\Gamma}{4}\right)^{\frac{1}{2}} exp\left(-\frac{\pi \mid \varepsilon_{g(e)} \mid}{\Gamma}\right), \qquad (31)$$

where D is the half bandwidth of the electrode density of states. The linewidth of the Kondo resonance is an energy scale called the Kondo temperature. The underlying mechanism behind the Kondo resonance is the occurrence of the cotunneling processes at ambient temperatures below $T_{K,g(e)}$. Simultaneous tunneling of two electrons with different spins results in an effective spin flip at the discrete levels.[19] This enables to lift the Coulomb blockade and generates a current flow between the two metal nanoparticles.

Once the Dyson equations are solved properly, the last step is to obtain the electrical current flowing through the discrete states within the quantum emitter. Following the earlier general formalism[20], the current flowing from the left or right nanoparticle to either $\mid g >$ or $\mid e >$ is given by[21]

$$I_{Lg(e)} = -2\bar{\Gamma}Re\int_{-\infty}^t dt_1 G_{g(e)}^<(t,t_1)b_{g(e)}(t_1,t)h(t-t_1)$$
$$+2\bar{\Gamma}Re\int_{-\infty}^t dt_1(g_{g(e)}(t,t_1)B_{g(e)}^<(t_1,t) + G_{g(e)}^<(t,t_1)$$
$$b_{g(e)}(t_1,t))f_L(t-t_1) \qquad (32)$$

and

$$I_{Rg(e)} = -2\bar{\Gamma}Re\int_{-\infty}^t dt_1 G_{g(e)}^<(t,t_1)b_{g(e)}(t_1,t)h(t-t_1)$$
$$+2\bar{\Gamma}Re\int_{-\infty}^t dt_1(g_{g(e)}(t,t_1)B_{g(e)}^<(t_1,t) + G_{g(e)}^<(t,t_1)$$
$$b_{g(e)}(t_1,t))f_R(t-t_1). \qquad (33)$$

In these expressions,

$$h(t - t_1) = \int_{-D}^{D} \frac{d\varepsilon}{2\pi} \rho(\varepsilon) e^{i\varepsilon(t-t_1)} \tag{34}$$

$$f_L(t - t_1) = \int_{-D}^{D} \frac{d\varepsilon}{2\pi} \rho(\varepsilon) \frac{e^{i\varepsilon(t-t_1)}}{1 + e^{\beta(\varepsilon - V/2)}} \tag{35}$$

$$f_R(t - t_1) = \int_{-D}^{D} \frac{d\varepsilon}{2\pi} \rho(\varepsilon) \frac{e^{i\varepsilon(t-t_1)}}{1 + e^{\beta(\varepsilon + V/2)}} \tag{36}$$

The net current through each level is equal to the difference between the left and right currents and can be written for a symmetrically coupled system as

$$I_{g(e)}(t) = 2\bar{\Gamma} Re \int_{-\infty}^{t} dt_1 (g_{g(e)}(t, t_1) B_{g(e)}^{<}(t_1, t) +$$
$$G_{g(e)}^{<}(t, t_1) b_{g(e)}(t_1, t))(f_L(t - t_1) - f_R(t - t_1)). \tag{37}$$

III. RESULTS AND DISCUSSION

We start by investigating the electrical current through a quantum emitter whose singly occupied discrete states lie at ε_g=-4.8 eV and ε_e=-1.6 eV with respect to the Fermi level of the metal nanoparticles. We refer to these set of parameters as system 1. This choice yields an emitter resonance energy of 3.2 eV which amounts to the energy gap between the two discrete states. During our calculations for the plasmon Green functions, we take the dipolar plasmon energy ε_p=3.49 eV, the laser bandwidth δ=1 meV and coupling of the dipolar plasmon to the laser $\gamma = 2\pi \mid W_0 \mid^2$=86 meV for the sake of consistency with the earlier optical absorption studies.[13,15]

We also assume that the left and right metal nanoparticles are identical and use parabolic density of states with D=9Γ in our calculations for simplicity. Furthermore, the coupling of the electrons in the discrete states to the metal nanoparticles are taken constant as $\bar{\Gamma}$=0.2 eV and Γ=0.8 eV. We want to note that we have the ability to incorporate the realistic band structure of the metal nanoparticles into our calculations[21–23]. Since this complexity significantly increases the computational cost, we leave it to the future studies.

We only explore the electrical current through $\mid e >$ because the electrical current flowing through $\mid g >$ remains zero for any attainable ambient temperature as long as the emitter resonance energy is around the dipolar plasmon energy since the Kondo temperature of $\mid g >$ is essentially zero in this case. Therefore, the only electrical current flowing in the circuit goes through $\mid e >$. The conductance of system 1 is depicted in Fig. 2 as a function of the ambient temperature for various values of the plasmon-exciton coupling Δ which is taken to be equal for the left and right metal nanoparticles due to the symmetry. We estimate that the Kondo temperature of $\mid e >$ is around 23 K for this system.
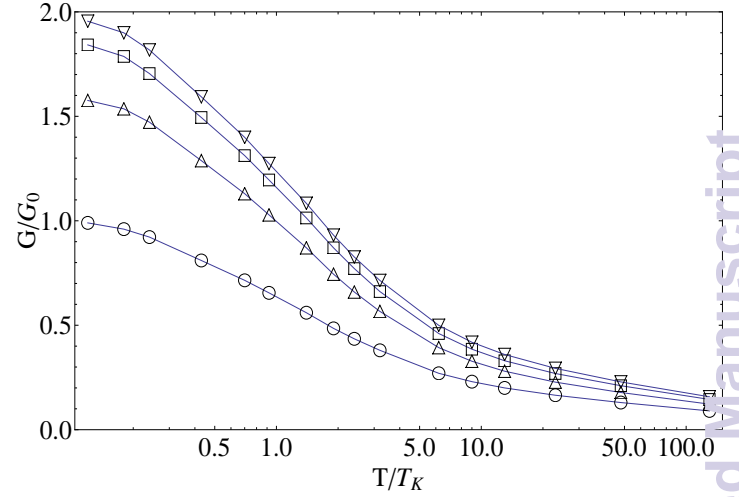

FIG. 2: This figure shows the electrical conductance through $\mid e >$ as a function of the ambient temperature for a plasmon-exciton coupling strength Δ=0 (empty circles), Δ=20 meV (empty triangles), Δ=40 meV (empty squares) and Δ=60 meV (empty inverted triangles) for system 1 at infinitesimal bias.
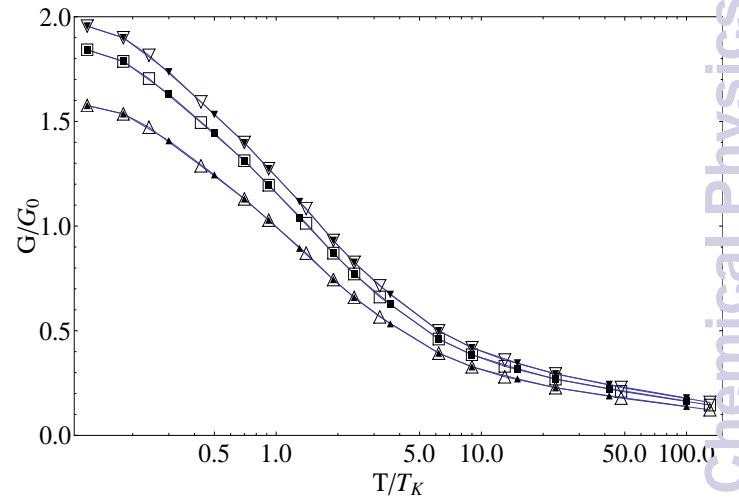

FIG. 3: This figure shows the electrical conductance through $\mid e >$ as a function of the ambient temperature for a plasmon-exciton coupling strength Δ=20 meV (empty triangles system 1, filled triangles system 2), Δ=40 meV (empty squares system 1, filled squares system 2) and Δ=60 meV (empty inverted triangles system 1, filled inverted triangles system 2) at infinitesimal bias.

Fig. 2 clearly shows that our conductance results in the absence of any plasmon-exciton coupling perfectly match the earlier results calculated for a single quantum dot in the Kondo regime.[24] This serves as a verification of the veracity of our approach. We then begin increasing the plasmon-exciton coupling gradually starting with Δ=20 meV used previously for optical absorption investigation.[15] It is obvious from Fig. 2 that

the finite plasmon-exciton coupling causes enhancement of the conductance at almost any ambient temperature with respect to the zero plasmon-exciton coupling case but the enhancement becomes particularly pronounced when the ambient temperature is around or falls below the Kondo temperature. We also boost the plasmon-exciton coupling to test the generality of the conductance enhancement. It can be easily seen from Fig. 2 that the conductance enhancement tends to increase with higher plasmon-exciton coupling values at any given ambient temperature. The most remarkable feature here is that the conductance saturates at twice the unitarity limit when the ambient temperature falls well below the Kondo temperature.
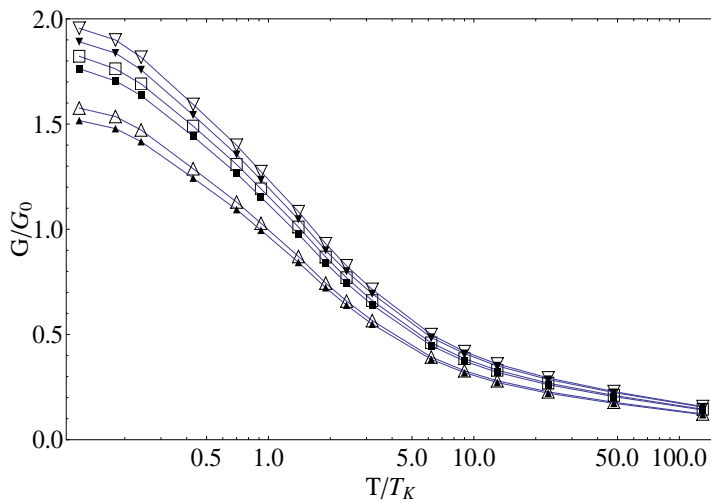

FIG. 4: This figure shows the electrical conductance through $| e >$ as a function of the ambient temperature for a plasmon-exciton coupling strength Δ=20 meV (empty triangles system 1, filled triangles system 3), Δ=40 meV (empty squares system 1, filled squares system 3) and Δ=60 meV (empty inverted triangles system 1, filled inverted triangles system 3) at infinitesimal bias.

We then study how the position of the discrete state $| e >$ with respect to the Fermi level of the metal nanoparticles alters the conductance results. Towards this end, we choose an emitter whose singly occupied discrete states are located at ε_g=-5.0 eV and ε_e=-1.8 eV. We refer to this configuration as system 2 which has the same emitter resonance energy with system 1. All other parameters for system 1 and 2 are kept identical and we carry out the conductance calculations for system 2 as a function of the ambient temperature. The results of this calculation are shown in Fig. 3 where we also superimpose the results from Fig. 2 for system 1. The Kondo temperature of ε_e in system 2 is estimated to be around 11 K. Therefore, we scale each system's results with respect to the Kondo temperature of ε_e in order to facilitate a direct comparison. One can quickly see from Fig. 3 the almost perfect scaling between the conductance results of system 1 and 2.

It is interesting to test whether changing the emitter resonance energy results in a deviation from the scaling we observe above. We choose an emitter with ε_g=-4.95 eV and ε_e=-1.6 eV for this purpose. We refer to this configuration as system 3 which has a slightly higher emitter resonance energy than system 1. We perform the conductance calculations through system 3 by keeping its other parameters the same as system 1. The results are shown in Fig. 4, where we also plot the data from system 1 as well for comparison. It is quite remarkable that an increase in the emitter resonance energy results in a drop in the conductance at temperatures below the Kondo temperature despite the fact that the Kondo temperature of $| e >$ is equal for both systems. On the other hand, the conductance difference between system 1 and 3 tends to decrease as the ambient temperature is increased and diminishes at temperatures much higher than the Kondo temperature.
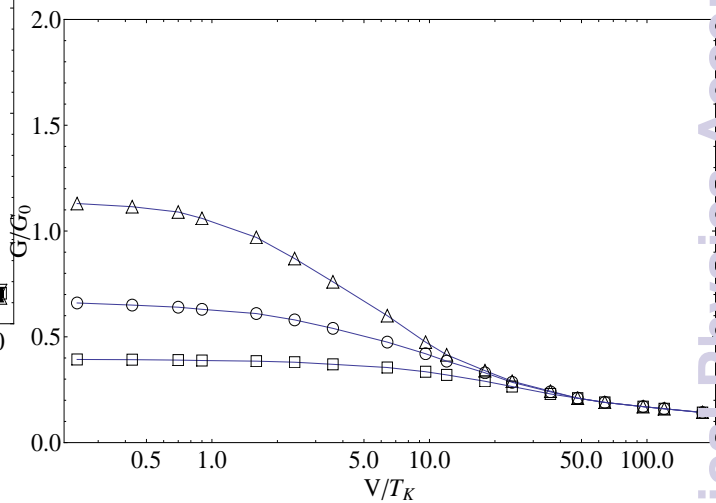

FIG. 5: This figure shows the electrical conductance through $| e >$ as a function of the voltage bias at T=0.7 T_K (empty triangles), T=2.4 T_K (empty circles) and T=6.2 T_K (empty squares) assuming a plasmon-exciton coupling strength Δ=20 meV for system 1.

So far, all our calculations pertain to the infinitesimal voltage bias between the metal nanoparticles. One may wonder how applying finite bias effects the conductance enhancement we observe due to the finite plasmon-exciton coupling. Fig. 5 shows the results of our conductance calculations as a function of the voltage bias for system 1 at three different ambient temperatures assuming a finite plasmon-exciton coupling. It is clear from this figure that increasing the voltage bias reduces the conductance at all ambient temperatures but this effect is much more dramatic at temperatures below the Kondo temperature since the finite bias inhibits the Kondo resonance by splitting it into two distinct peaks located at each nanoparticle's Fermi level.[24] Consequently, we can conclude that the finite bias tends to curb the conductance enhancement caused by the finite plasmon-exciton

coupling to an extent that depends on the ambient temperature.

We repeat the conductance calculations of Fig. 5 for system 1 by using the same ambient temperatures and assuming a higher plasmon-exciton coupling in order to test the robustness of the reduction in the conductance enhancement. Our results are displayed in Fig. 6, which clearly demonstrates that the reduction in the conductance enhancement upon increasing the voltage bias is applicable to elevated values of plasmon-exciton coupling as well. In fact, one can easily see that the enhancement in the conductance gets quenched more rapidly at temperatures below the Kondo temperature when the plasmon-exciton coupling increases.
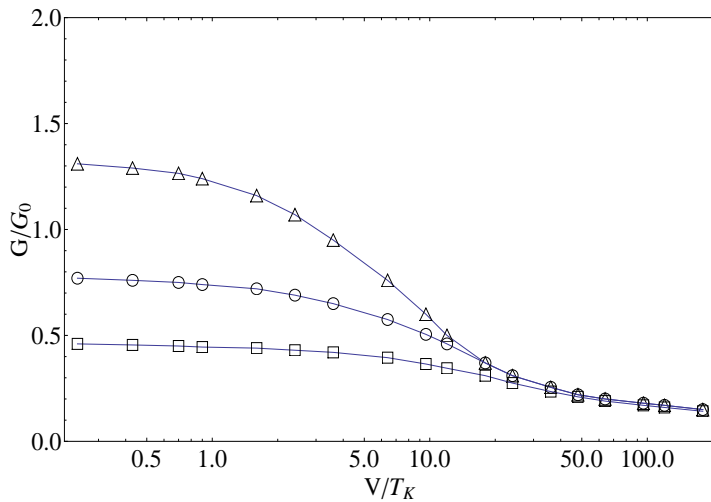

FIG. 6: This figure shows the electrical conductance through $| e >$ as a function of the voltage bias at $T=0.7$ T_K (empty triangles), $T=2.4$ T_K (empty circles) and $T=6.2$ T_K (empty squares) assuming a plasmon-exciton coupling strength $\Delta=40$ meV for system 1.

All these observations suggest that the conductance enhancement due to the finite plasmon-exciton coupling is somehow intrinsically related to the existence of the Kondo resonance in the density of states of $| e >$ because the enhancement starts to dwindle once the Kondo resonance gets inhibited gradually. Therefore, it is important to put forward a microscopic scenario to elucidate our conductance calculations. The electron transport mechanism is relatively straightforward in the absence of any plasmon-exciton coupling. In this case, the flow of electrons occurs solely through $| e >$ via spin flips in the cotunneling regime. Since $| g >$ lies too far away from the Fermi level of the metal nanoparticles, it remains firmly Coulomb blockaded. Consequently, it cannot contribute to the electron transport at all. This is identical to the case where a single quantum dot is attached to two metallic leads.[24] There is only one channel available for the electron transport and the conductance saturates at one quantum of conductance G_0 when the ambient temperature falls well below the Kondo temperature. Unsur-

prisingly, we recover those results precisely ignoring any plasmon-exciton coupling as one can see in Fig. 2.
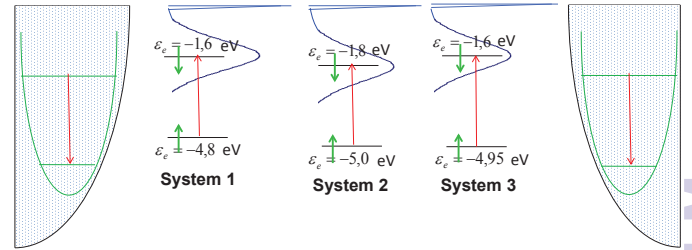

FIG. 7: This figure schematically shows the three systems 1,2 and 3 discussed in the text and illustrates the mechanism of Kondo resonance formed at $| e >$ via the spin flips mediated through the plasmon-exciton coupling.

The situation becomes more complicated when the plasmon-exciton coupling is turned on. An electron occupying $| g >$ must be able to jump to $| e >$ when the plasmon is annihilated in one of the metal nanoparticles or vice versa for this mechanism to be active. Since the double occupancy is forbidden in each discrete level, this process is not possible in the sequential tunneling regime. Consequently, the plasmon-exciton coupling is unable to contribute to the electron transport unless the Kondo effect starts to play a role. On the other hand, the spin flip processes taking place at $| e >$ becomes possible when the ambient temperature approaches or falls below the Kondo temperature of $| e >$. In this cotunneling regime, annihilation of the plasmon in one of the metal nanoparticles can trigger the tunneling of an electron from $| g >$ to $| e >$ if an electron with the opposite spin vacates $| e >$ momentarily by tunneling to one of the metal nanoparticles. Fig. 7 depicts the spin flip mechanism and the ensuing Kondo resonance at $| e >$ due to the plasmon-exciton coupling alongside with the configurations of the quantum emitter corresponding to systems 1,2 and 3. This process arising purely due to the plasmon-exciton coupling generates additional electron flow across the metal nanoparticles by opening up a new transport channel. This is why we see the saturation of the conductance at twice the quantum of conductance at temperatures well below the Kondo temperature of $| e >$.

The solution of the Dyson equations rely on the self-energy terms which involve the plasmon Green functions as well as the pseudofermion and slave boson Green functions. The electron transport mechanism which is governed by the solution of the Dyson equations depends on the formation and existence of the Kondo resonance in

the density of states of $|e>$ as well as the emitter resonance energy crucially because the emitter resonance energy influences the position and shape of the Fano resonance in the optical absorption spectrum.[15] This is reflected in the plasmon Green functions which come into play in our electron transport calculations by appearing in the self-energy terms of each Dyson equation. Systems 1 and 2 both have the same emitter resonance energy pinning their Fano resonance to the same spot in the optical absorption spectrum.[15] Consequently their optical absorption spectrums which involve the convolution of the Fourier transform of the plasmon Green function with the laser induced mode population show universal scaling with respect to the Kondo temperature of $|e>$.[13] The slave-boson and pseudofermion Green functions which originate from the solutions of separate single quantum dot problems are the only other factors appearing in the self-energy terms of Dyson equations and the electron transport has also been shown to exhibit universal scaling with respect to the Kondo temperature for a single quantum dot problem previously.[18,24] Therefore, it should be expected that the conductance curves of system 1 and 2 also overlap after scaling with respect to the Kondo temperature of $|e>$ and this is indeed precisely what we observe in Fig. 3. This universal scaling of quantum transport in the Kondo regime has also been observed experimentally for various single molecule devices utilizing C_{60} and Cu-containing transition metal complex as the active element[25] albeit in the absence of any plasmon-exciton coupling.

On the other hand, the conductance curves for systems 1 and 3 differ slightly at temperatures around or below the Kondo temperature of $|e>$ but start overlapping at high temperatures. This is again due to the difference in the position and shape of the Fano resonance in the optical absorption spectrum of the two systems. However, once the Kondo resonance starts to diminish at high temperatures so does the Fano resonance in the optical absorption spectrum[13] and the optical absorption spectrum of both systems consists of nothing but a plasmon resonance at elevated temperatures. This makes the plasmon Green functions identical for systems 1 and 3 and the overlap in the conductance curves is recovered in this limit.

The advantage of having low temperature samples is to be able to investigate the influence of the spin flip dynamics associated with the formation of the Kondo resonance at or below the Kondo temperature on the electron transmission. The low ambient temperatures below the Kondo temperature reported in this paper can be accessed in an experiment by immersing the whole system in a cryostat.[25] Bringing the discrete states of the quantum emitter closer to the Fermi level of the nanoparticles via a gate voltage constitutes a possible remedy for this difficulty since it increases the Kondo temperature. All the reported ambient temperatures also increase in this situation due to the scaling and this can reduce the reliance on a cryostat somewhat. Moreover, the formation of plasmons in metal nanoparticles requires illumination by a laser. This naturally leads to heating and may also be a serious impediment to reduce the ambient temperatures to the desired level experimentally. It has previously been shown that this inherent problem can be circumvented by using a laser whose pulse duration is much longer than 100 ps.[26] This helps to diffuse the heat to the environment, thereby curtailing the temperature rise in the molecule-metal nanoparticle dimer system considerably.

IV. CONCLUSION

In this paper, we investigated the electrical current flowing through a Coulomb blockaded quantum emitter coupled to plasmonic metal nanoparticles by developing a novel many body theory for the first time. We found that the plasmon-exciton coupling can serve as an enhancement for the conductance through this device by opening up a new transport channel at temperatures around or below the Kondo temperature of the discrete state lying closer to the Fermi level of the metal nanoparticles. It turned out the application of finite bias between the metal nanoparticles and increasing the emitter resonance energy tends to suppress this enhancement. We proposed a detailed microscopic scheme to account for these peculiarities based on the spin flip processes which give rise to an intricate many body state called the Kondo effect. We hope that our pioneering work will provide further excitement and motivation to carry out experiments at cryogenic temperatures which will hopefully provide a better understanding of plexcitonic systems.

V. ACKNOWLEDGMENTS

[1] Lal S, Link S and Halas N J 2007 *Nat. Photonics* **1** 641–648
[2] Schuller J A, Barnard E S, Cai W, Jun Y C, White J S and Brongersma M L 2010 *Nat. Mater.* **9** 193–204
[3] Awschalom D D, Bassett L C, Dzurak A S, Hu E L and Petta J R 2013 *Science* **339** 1174–1179
[4] Fofang N T, Park T H, Neumann O, Mirin N A, Nordlander P and Halas N J 2008 *Nano Lett.* **8** 3481–3487
[5] Wurtz G A, Evans P R, Hendren W, Atkinson R, Dickson W, Pollard R J, Zayats A V, Harrison W and Bower C 2007 *Nano Lett.* **7** 1297–1303
[6] Zheng Y B, Kiraly B, Cheunkar S, Huang T J and Weiss P S 2011 *Nano Lett.* **11** 2061–2065

[7] Luk'yanchuk B, Zheludev N I, Maier S A, Halas N J, Nordlander P, Giessen H and Chong C T 2010 *Nat. Mater.* **9** 707–715

[8] Song P, Nordlander P and Gao S 2011 *J. Chem. Phys.* **134** 074701

[9] Esteban R, Borisov A G, Nordlander P and Aizpurua J 2012 *Nature Commun.* **3** 825

[10] Delga A, Feist J, Bravo-Abad J and Garcia-Vidal F J 2014 *J. Opt.* **16** 114018

[11] Delga A, Feist J, Bravo-Abad J and Garcia-Vidal F J 2014 *Phys. Rev. Lett.* **112** 253601

[12] Feist J and Garcia-Vidal F J 2015 *Phys. Rev. Lett.* **114** 196402

[13] Goker A 2015 *Phys. Chem. Chem. Phys.* **17** 11569–11576

[14] Vadai M, Nachman N, Ben-Zion M, Burkle M, Pauly F, Cuevas J C and Selzer Y 2013 *J. Phys. Chem. Lett.* **4** 2811–2816

[15] Manjavacas A, de Abajo F J G and Nordlander P 2011 *Nano Lett.* **11** 2318–2323

[16] Shao H X, Langreth D C and Nordlander P 1994 *Phys. Rev. B* **49** 13929–13947

[17] Aguado R and Langreth D C 2003 *Phys. Rev. B* **67** 245307

[18] Izmaylov A F, Goker A, Friedman B A and Nordlander P 2006 *J. Phys.: Condens. Matter* **18** 8995–9006

[19] Kondo J 1964 *Prog. Theor. Phys.* **32** 37

[20] Jauho A P, Wingreen N S and Meir Y 1994 *Phys. Rev. B* **50** 5528

[21] Goker A, Friedman B A and Nordlander P 2007 *J. Phys.: Condens. Matter* **19** 376206

[22] Goker A, Zhu Z Y, Manchon A and Schwingenschlogl U 2011 *Chem. Phys. Lett.* **509** 48

[23] Goker A, Zhu Z Y, Manchon A and Schwingenschlogl U 2010 *Phys. Rev. B* **82** 161304(R)

[24] Plihal M, Langreth D C and Nordlander P 2005 *Phys. Rev. B* **71** 165321

[25] Scott G D, Keane Z K, Ciszek J W, Tour J M and Natelson D 2009 *Phys. Rev. B* **79** 165413

[26] Luk'yanchuk B S, Miroshnichenko A E, Tribelsky M I, Kivshar Y S and Khokhlov A R 2012 *New J. Phys* **14** 093022

APPENDIX A: SELF-ENERGIES AND THEIR PROJECTION

The self energy of a pseudofermion within the quantum emitter due to the plasmon-exciton coupling is shown in Fig. 8. On the other hand, the self-energy of a pseudofermion due to emitter-nanoparticle coupling is shown in panel a of Fig. 10. Based on these diagrams, the unprojected lesser and greater pseudofermion self-energies for a pseudofermion residing in $\mid g >$ can be written as a sum of contributions from panels a of Fig. 8 and Fig. 10, yielding

$$\Sigma_g^<(t,t') = K_g^<(t,t')B_g^<(t,t') + \mid \Delta \mid^2 G_e^<(t,t')B_g^<(t,t') \\ \times B_e^>(t',t)P^>(t',t), \qquad (A1)$$

$$\Sigma_g^>(t,t') = K_g^>(t,t')B_g^>(t,t') + \mid \Delta \mid^2 G_e^>(t,t')B_g^>(t,t') \\ \times B_e^<(t',t)P^<(t',t). \qquad (A2)$$
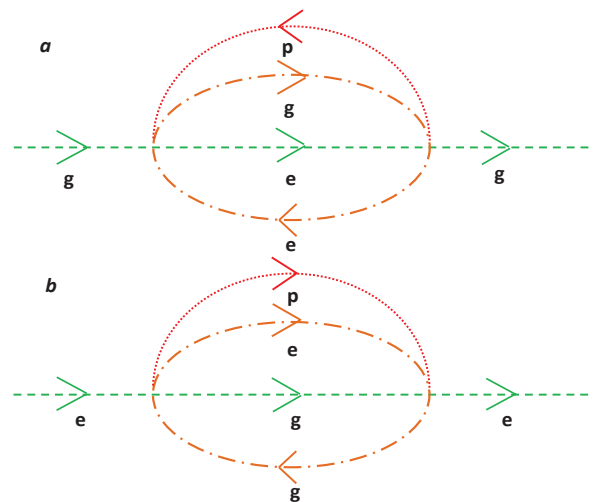

FIG. 8: This figure illustrates the self energy of the pseudofermion propagator arising due to the plasmon-exciton coupling. Red (dotted) lines represent the plasmon propagator, whereas orange (dot-dashed) and green (dashed) lines denote the slave boson and the pseudofermion propagators. Panel a and b depict the self-energy of a pseudofermion residing in $\mid g >$ and $\mid e >$ respectively.

Similarly, the summation of contributions from panel b of Fig. 8 and panel a of Fig. 10 yield the unprojected lesser and greater self energies for a pseudofermion residing in $\mid e >$ as

$$\Sigma_e^<(t,t') = K_e^<(t,t')B_e^<(t,t') + \mid \Delta \mid^2 G_g^<(t,t')B_e^<(t,t') \\ \times B_g^>(t',t)P^<(t,t'), \qquad (A3)$$

$$\Sigma_e^>(t,t') = K_e^>(t,t')B_e^>(t,t')+ \mid \Delta \mid^2 G_g^>(t,t')B_e^>(t,t')$$
$$\times B_g^<(t',t)P^>(t,t'). \tag{A4}$$

Since the retarded pseudo-fermion self-energy is defined as

$$\Sigma_{g(e)}^r(t,t') := -i\Theta(t-t')(\Sigma_{g(e)}^>(t,t')+\Sigma_{g(e)}^<(t,t')), \tag{A5}$$

a few algebraic manipulations give the unprojected retarded pseudo-fermion self-energies as

$$\begin{aligned}
\Sigma_g^r(t,t') =\ & K_g^>(t,t')B_g^r(t,t') + K_g^r(t,t')B_g^<(t,t') \\
& + \mid \Delta \mid^2 [G_e^>(t,t')B_g^r(t,t')B_e^<(t',t)P^<(t',t) \\
& + G_e^r(t,t')B_g^<(t,t')B_e^>(t',t)P^>(t',t) \\
& + G_e^>(t,t')B_g^<(t,t')B_e^<(t',t)P^a(t',t) \\
& + G_e^>(t,t')B_g^<(t,t')B_e^a(t',t)P^>(t',t)]
\end{aligned} \tag{A6}$$

and

$$\begin{aligned}
\Sigma_e^r(t,t') =\ & K_e^>(t,t')B_e^r(t,t') + K_e^r(t,t')B_e^<(t,t') \\
& + \mid \Delta \mid^2 [G_g^>(t,t')B_e^r(t,t')B_g^<(t',t)P^>(t,t') \\
& + G_g^r(t,t')B_e^<(t,t')B_g^>(t',t)P^<(t,t') \\
& + G_g^>(t,t')B_e^<(t,t')B_g^a(t',t)P^>(t,t') \\
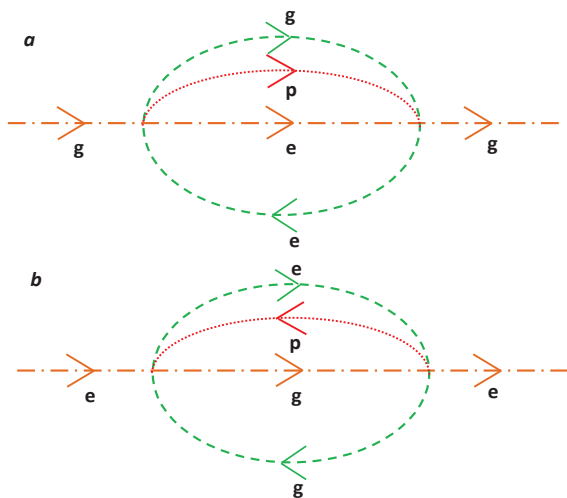& + G_g^>(t,t')B_e^<(t,t')B_g^>(t',t)P^r(t,t')].
\end{aligned} \tag{A7}$$

FIG. 9: This figure illustrates the self energy of the slave boson propagator arising due to the plasmon-exciton coupling. Red (dotted) lines represent the plasmon propagator, whereas orange (dot-dashed) and green (dashed) lines denote the slave boson and the pseudofermion propagators. Panel a and b depict the self-energy of a slave boson residing in $\mid g >$ and $\mid e >$ respectively.

The self energy of a slave-boson within the emitter due to the plasmon-exciton coupling is shown in Fig. 9.

Moreover, the self-energy of a slave-boson due to emitter-nanoparticle coupling is shown in panel b of Fig. 10. Hence, the unprojected lesser and greater slave-boson self-energies for a slave-boson residing in $\mid g >$ can be written as a sum of contributions from panel a of Fig. 9 and panel b of Fig. 10, yielding

$$\Pi_g^<(t,t') = K_g^>(t',t)G_g^<(t,t')+ \mid \Delta \mid^2 B_e^<(t,t')P^<(t,t')$$
$$\times G_g^<(t,t')G_e^>(t',t). \tag{A8}$$

$$\Pi_g^>(t,t') = K_g^<(t',t)G_g^>(t,t')+ \mid \Delta \mid^2 B_e^>(t,t')P^>(t,t')$$
$$\times G_g^>(t,t')G_e^<(t',t). \tag{A9}$$

In a similar fashion, the summation of contributions from panel b of Fig. 9 and panel b of Fig. 10 yield the unprojected lesser and greater self energies for a slave-boson in $\mid e >$ as

$$\Pi_e^<(t,t') = K_e^>(t',t)G_e^<(t,t')+ \mid \Delta \mid^2 B_g^<(t,t')P^>(t',t)$$
$$\times G_e^<(t,t')G_g^>(t',t). \tag{A10}$$

$$\Pi_e^>(t,t') = K_e^<(t',t)G_e^>(t,t')+ \mid \Delta \mid^2 B_g^>(t,t')P^<(t',t)$$
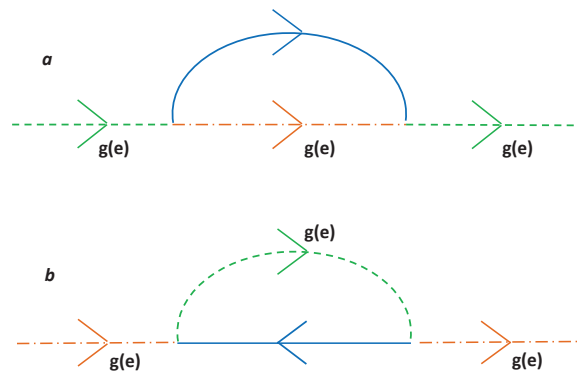$$\times G_e^>(t,t')G_g^<(t',t). \tag{A11}$$

FIG. 10: Panel a and b of this figure illustrate the self energy of each state's pseudofermion and slave boson propagator respectively due to the emitter-nanoparticle coupling. Green (dashed) lines represent the pseudofermion propagator, whereas orange (dot-dashed) and blue (solid) lines denote the slave boson propagator for the same state and the electron propagator in the nanoparticle to which the pseudofermion tunnels respectively.

The retarded slave boson self-energy is defined as

$$\Pi_{g(e)}^r(t,t') := -i\Theta(t-t')(\Pi_{g(e)}^>(t,t') - \Pi_{g(e)}^<(t,t')). \tag{A12}$$

After some manipulations, we end up with the unprojected retarded slave-boson self-energies as

$$
\begin{aligned}
\Pi_g^r(t,t') &= K_g^<(t',t)G_g^r(t,t') + K_g^a(t',t)G_g^<(t,t') \\
&+ |\Delta|^2 \left[G_g^>(t,t')B_e^r(t,t')G_e^<(t',t)P^>(t,t') \right. \\
&- G_g^r(t,t')B_e^<(t,t')G_e^>(t',t)P^<(t,t') \\
&- G_g^>(t,t')B_e^<(t,t')G_e^a(t',t)P^>(t,t') \\
&\left. - G_g^>(t,t')B_e^<(t,t')G_e^>(t',t)P^r(t,t') \right]
\end{aligned} \tag{A13}
$$

and

$$
\begin{aligned}
\Pi_e^r(t,t') &= K_e^<(t',t)G_e^r(t,t') + K_e^a(t',t)G_e^<(t,t') \\
&+ |\Delta|^2 \left[G_e^>(t,t')B_g^r(t,t')G_g^<(t',t)P^<(t',t) \right. \\
&- G_e^r(t,t')B_g^<(t,t')G_g^>(t',t)P^>(t',t) \\
&- G_e^>(t,t')B_g^<(t,t')G_g^a(t',t)P^<(t',t) \\
&\left. - G_e^>(t,t')B_g^<(t,t')G_g^>(t',t)P^a(t',t) \right].
\end{aligned} \tag{A14}
$$

$K_{g(e)}^>(t,t')$ and $K_{g(e)}^<(t,t')$ appearing in these expressions are defined in terms of the density of states of the metal nanoparticles with a half bandwidth of D as

$$
\begin{aligned}
K_{g(e)}^<(t,t') &= \bar{\Gamma}_{tot,g(e)} \int_{-D}^{D} \frac{d\varepsilon}{2\pi} \rho(\varepsilon) \frac{1}{1+e^{\beta\varepsilon}} e^{i\varepsilon(t-t')} \\
K_{g(e)}^>(t,t') &= \bar{\Gamma}_{tot,g(e)} \int_{-D}^{D} \frac{d\varepsilon}{2\pi} \rho(\varepsilon) \frac{e^{\beta\varepsilon}}{1+e^{\beta\varepsilon}} e^{i\varepsilon(t-t')}
\end{aligned} \tag{A15}
$$

where β denotes the inverse of the ambient temperature and we define

$$
\begin{aligned}
\bar{\Gamma}_{tot,g(e)} &= \bar{\Gamma}_{L,g(e)} + \bar{\Gamma}_{R,g(e)} \\
&= 2\pi(|V_{L,g(e)}(\varepsilon_f)|^2 + |V_{R,g(e)}(\varepsilon_f)|^2)
\end{aligned} \tag{A16}
$$

with ε_f representing the Fermi level of the metal nanoparticles. Tunneling matrix elements are assumed to be time and energy independent yielding $V_{K,g(e)}(\varepsilon) = V_{K,g(e)}(\varepsilon_f)$. We also assume that each discrete state is symmetrically and equally coupled to metal nanoparticles such that $V_{K,g(e)} = V_{K',g(e)} = V_{K',e(g)}$. This also means that $\bar{\Gamma}_{L,g(e)} = \bar{\Gamma}_{R,g(e)} = \bar{\Gamma}$. Consequently, we will drop the subscripts from $K_{g(e)}^>(t,t')$ and $K_{g(e)}^<(t,t')$ from now on and denote them simply as $K^>(t,t')$ and $K^<(t,t')$. Moreover, we take $\Gamma(\varepsilon) = \bar{\Gamma}\rho(\varepsilon)$ and use Γ as the value of $\Gamma(\varepsilon)$ at ε_f.

We now need to project the lesser, greater and retarded self energies into $Q_{B,g(e)} = 1$ subspace. In order to put our equations in a compact form, we will introduce

$$
\begin{aligned}
B_{g(e)}^r(t,t') &= -i\Theta(t-t') \left[B_{g(e)}^>(t,t') - B_{g(e)}^<(t,t') \right] \\
&:= -i\Theta(t-t')b_{g(e)}(t,t')
\end{aligned} \tag{A17}
$$

for the slave boson retarded Green functions. This implies

$$
B_{g(e)}^>(t,t') = b_{g(e)}(t,t') + B_{g(e)}^<(t,t'). \tag{A18}
$$

Identical representation for the pseudofermion retarded Green functions gives

$$
\begin{aligned}
G_{g(e)}^r(t,t') &= -i\Theta(t-t') \left[G_{g(e)}^>(t,t') + G_{g(e)}^<(t,t') \right] \\
&:= -i\Theta(t-t')g_{g(e)}(t,t').
\end{aligned} \tag{A19}
$$

Consequently, we obtain

$$
G_{g(e)}^>(t,t') = g_{g(e)}(t,t') - G_{g(e)}^<(t,t'). \tag{A20}
$$

The Green functions have to be calculated by plugging the corresponding projected self-energies into the relevant Dyson equation. To obtain these projected self-energies, we need to maintain the same charge dependency on both sides of the Dyson equations. Projections have to be performed for each discrete energy level independently by taking into account Eq. (10). We want to note that the retarded pseudofermion and and slave-boson Green functions are of the order $Q_{B,g(e)}^0$ while the less than ones are of the order $Q_{B,g(e)}^1$. When one of the less than Green functions appears on the l.h.s. of a Dyson equation for $|g>$ or $|e>$, r.h.s. must be modified such that it is also of the order $Q_{B,g(e)}^1$ by utilizing the relations in Eq. (A17,A18,A19,A20).

We can consider the Dyson equation in Eq. (19) for $|g>$ to demonstrate explicitly how the projection procedure is applied. Since l.h.s. of this equation scales with $Q_{B,g}^1$ we need to modify the r.h.s. accordingly where retarded and less than self-energy expressions play a role. After inserting Eq. (A6) into Eq. (19) we see that the less than slave boson Green function for $|g>$ whose charge dependency is $Q_{B,g}^1$ appears in several terms. Consequently, the related lines multiplying with this Green function have to be removed. Meantime, the greater than pseudofermion Green function for $|e>$ in one of the remaning lines has to be transformed into zero charge dependency by invoking Eq. (A20). In this arrangement, the less than slave boson Green function for $|e>$ multiplies the less than pseudofermion Green function for $|e>$ in this term. We have to drop the latter one in order to reduce the charge dependency to $Q_{B,e}^1$ on the r.h.s. We want to emphasize that this truncation is required and is not an additional approximation.[17] Similar treatment is required for the second term on the r.h.s. of Eq. (19) using the less than pseudofermion self-energy expression for $|g>$ given by Eq. (A1).

Moreover, the pseudo-fermion and slave boson Green functions within the self-energy expressions have to be calculated in the absence of any coupling between the discrete states $|g>$ and $|e>$ following the previous work.[17] This implies that these Green functions have to be calculated by solving the Dyson equations for two independent impurities in the absence of any plasmon-exciton coupling.[17] This is required in order not to take into account the plasmon-exciton coupling twice, namely to avoid the double counting problem. From now on, we denote these Green functions with a tilde on top to differentiate them. These adjustments give us the projected pseudofermion self-energies as

$$\Sigma_g^<(t,t') = K^<(t,t')\tilde{B}_g^<(t,t') +$$
$$| \Delta |^2 \tilde{G}_e^<(t,t')\tilde{B}_g^<(t,t')\tilde{b}_e(t,t')P^>(t',t), \quad \text{(A21)}$$

$$\Sigma_g^r(t,t') = K^>(t,t')\tilde{B}_g^r(t,t') +$$
$$| \Delta |^2 \tilde{g}_e(t,t')\tilde{B}_g^r(t,t')\tilde{B}_e^<(t',t)P^<(t',t). \quad \text{(A22)}$$

$$\Sigma_e^<(t,t') = K^<(t,t')\tilde{B}_e^<(t,t') +$$
$$| \Delta |^2 \tilde{G}_g^<(t,t')\tilde{B}_e^<(t,t')\tilde{b}_g(t,t')P^<(t,t'), \quad \text{(A23)}$$

$$\Sigma_e^r(t,t') = K^>(t,t')\tilde{B}_e^r(t,t') +$$
$$| \Delta |^2 \tilde{g}_g(t,t')\tilde{B}_e^r(t,t')\tilde{B}_g^<(t',t)P^>(t',t). \quad \text{(A24)}$$

Similarly the projected slave-boson self energies are given by

$$\Pi_g^<(t,t') = K^>(t',t)\tilde{G}_g^<(t,t') +$$
$$| \Delta |^2 \tilde{B}_e^<(t,t')\tilde{G}_g^<(t,t')\tilde{g}_e(t',t)P^<(t,t'), \quad \text{(A25)}$$

$$\begin{aligned}
\Pi_g^r(t,t') =\ & K^<(t',t)\tilde{G}_g^r(t,t') \\
& + | \Delta |^2 [\tilde{g}_g(t,t')\tilde{B}_e^r(t,t')\tilde{G}_e^<(t',t)P^>(t,t') \\
& -\tilde{G}_g^r(t,t')\tilde{B}_e^<(t,t')\tilde{g}_e(t',t)P^<(t,t') \\
& -\tilde{g}_g(t,t')\tilde{B}_e^<(t,t')\tilde{G}_e^a(t',t)P^>(t,t') \\
& -\tilde{g}_g(t,t')\tilde{B}_e^<(t,t')\tilde{g}_e(t',t)P^r(t,t')]. \quad \text{(A26)}
\end{aligned}$$

and

$$\begin{aligned}
\Pi_e^<(t,t') =\ & K^>(t',t)\tilde{G}_e^<(t,t') + | \Delta |^2 \tilde{B}_g^<(t,t')\tilde{G}_e^<(t,t') \\
& \times \tilde{g}_g(t',t)P^>(t',t), \quad \text{(A27)}
\end{aligned}$$

$$\begin{aligned}
\Pi_e^r(t,t') =\ & K^<(t',t)\tilde{G}_e^r(t,t') \\
& + | \Delta |^2 [\tilde{g}_e(t,t')\tilde{B}_g^r(t,t')\tilde{G}_g^<(t',t)P^<(t',t) \\
& -\tilde{G}_e^r(t,t')\tilde{B}_g^<(t,t')\tilde{g}_g(t',t)P^>(t',t) \\
& -\tilde{g}_e(t,t')\tilde{B}_g^<(t,t')\tilde{G}_g^a(t',t)P^<(t',t) \\
& -\tilde{g}_e(t,t')\tilde{B}_g^<(t,t')\tilde{g}_g(t',t)P^a(t,t')]. \quad \text{(A28)}
\end{aligned}$$